catalysts

MDPI

Article

Synergically Improving Light Harvesting and Charge Transportation of TiO_2 Nanobelts by Deposition of MoS_2 for Enhanced Photocatalytic Removal of Cr(VI)

Jie Liu [1], Ying Li [1], Jun Ke [2,*], Zhong Wang [3] and Huining Xiao [1,*]

1. School of Environmental Science and Engineering, North China Electric Power University, Baoding 071003, China; liujieshuiwen@gmail.com (J.L.); liyingncepc@gmail.com (Y.L.)
2. School of Chemistry and Environmental Engineering, Wuhan Institute of Technology, Wuhan 430072, China
3. Key Laboratory of Biofuels, Qingdao Institute of Bioenergy and Bioprocess Technology, Chinese Academy of Sciences, Qingdao 266101, China; wangzhong@qibebt.ac.cn

* Correspondence: jke@wit.edu.cn (J.K.); hnxiao@ncepu.edu.cn (H.X.); Tel.: +86-27-8719-4560 (J.K.); +86-312-7525-530 (H.X.)

Academic Editors: Shaobin Wang and Xiaoguang Duan
Received: 16 December 2016; Accepted: 3 January 2017; Published: 19 January 2017

Abstract: Herein, MoS_2/TiO_2 nanobelts heterojunction have been successfully synthesized by in situ growth method for photocatalytic reduction of Cr(VI). TiO_2 nanobelts (NBs) with rough surface were prepared firstly by acidic treatment process, which is beneficial for deposition and growth of MoS_2 to form heterojunctions. As a result of special energy level offset and nanostructure, MoS_2/TiO_2 NBs composite were endowed with higher light-harvesting capacity and charge transportation efficiency, which are indispensible merits for excellent photocatalytic activity. The photocatalytic reduction of Cr(VI) reveals that the synthesized MoS_2/TiO_2 NBs composite have superior photocatalytic ability than other samples. Meanwhile, a photoreduction mechanism is proposed based on the systematic investigation, where the photogenerated electrons are demonstrated as the dominant reductive species to reduce Cr(VI) to Cr(III).

Keywords: environmental remediation; Cr(VI); photocatalysis; TiO_2 NBs; MoS_2

1. Introduction

Hexavalent chromium (Cr(VI)) is a common heavy metal pollutant in the wastewater, which has attracted considerable attention around the world owing to its high toxicity and strong carcinogenic activity for humans and living things in nature [1–3]. Therefore, it is of great importance to explore how to effectively remove Cr(VI) in wastewater. Semiconductor-based photocatalytic reduction of Cr(VI) has received much attention recently due to its low cost, sustainability, and environmental friendliness without secondary pollution [4–7]. Nevertheless, to date, developing a highly efficient, cost-effective and stable photocatalyst for removal of Cr(VI) with visible-light activity is still being pursued.

Among various metal oxide semiconductors, TiO_2 is probably one of the most studied oxide semiconductor materials, and is used in a broad range of applications such as paints [8], (photo)catalysis [9], photovoltaics [10], and hybrid light-emitting diodes [11], and, as aforementioned, alkaliion batteries [12]. Owing to polymorphism richness of TiO_2 and its $3d^0$ electronic configuration inducing exceptional sensitiveness of the optoelectronic properties to the introduction of point defects, it has been extensively studied and endowed with new properties [13–15]. However, similar to many semiconductors, the poor harvesting of solar energy and charge carrier separation of pure TiO_2 leads to the low photocatalytic activity and thus cannot meet the demand of commercial applications.

To improve the photocatalytic performance of TiO_2, coupling TiO_2 with other semiconductors for constructing a heterojunction system is an interesting method that has received more attention in the past decades [16–20]. Graphene-like molybdenum disulfide (MoS_2) can be a good candidate for tuning photoresponse and improving charge carrier transportation properties [21–24]. In fact, layered MoS_2 is often used as an effective cocatalyst in photocatalytic or electrocatalytic hydrogen evolution reactions due to its large surface area and high electrical conductivity [25–27]. These studies demonstrate that the incorporation of layered MoS_2 with a metal oxide can strongly promote visible light harvest ability and separation efficiency of excited charges and photocatalytic activity.

Based on the above strategy, herein, by means of coupling TiO_2 nanobelts with MoS_2, we successfully fabricated MoS_2/TiO_2 NBs composite to form a *p-n* heterojunction for improving efficiency of solar energy utilization and photoinduced charge transportation. The photocatalytic reduction of Cr(VI) reveals that the synthesized MoS_2/TiO_2 NBs composite have superior photocatalytic ability than other samples. As a result of special energy level offset and nanostructure, MoS_2/TiO_2 NBs composite were endowed with higher light-harvesting capacity and charge transportation efficiency, which are indispensible merits for excellent photocatalytic activity. Meanwhile, a photoreduction mechanism is proposed based on the systematic investigation, where the photogenerated electrons are demonstrated as the dominant reductive species to reduce Cr(VI) to Cr(III).

2. Results and Discussion

2.1. Synthesis and Characterizations of MoS_2/TiO_2 NBs Heterojunction Composite

The crystallographic structure and phase of the as-obtained pristine TiO_2 NBs, MoS_2, and MoS_2/TiO_2 heterojunction samples were examined by XRD analysis, as shown in Figure 1. All the diffraction peaks of the TiO_2 NBs sample can be well matched with anatase phase of TiO_2 (Joint Committee on Powder Diffraction Standards (JCPDS) card no. 21-1272) [28]. No impurity peaks are detected, implying that the final TiO_2 product is of pure phase. The strong peaks at 25.2°, 37.7°, 48.0°, 53.9°, 55.0°, and 62.7° are attributed to the (101), (400), (200), (105), (211), and (204) crystal facets, respectively [29]. In the case of MoS_2 nanotubes, the XRD pattern is agreement with hexagonal phase of MoS_2 (JCPDS card no. 73-1508), whereas the crystallinity of MoS_2 nanotubes is relatively low, resulting in broadened diffraction peaks due to lack of high temperature annealing. As shown in Figure 1, three obvious peaks at 16.4°, 32.7°, and 56.9° are ascribed to the characteristic (002), (100), and (110) facets, respectively [30,31]. After in situ growth of MoS_2 by means of adding TiO_2 as a precursor, the characteristic diffraction peaks of MoS_2 and TiO_2 can be observed in the XRD pattern of the as-obtained composite in Figure 1, which indicates that MoS_2 and TiO_2 exist together in the composite. Meanwhile, we can find that the relative intensity of diffraction peaks due to MoS_2 is lower than that of TiO_2 despite designed molar ratio of TiO_2 and Mo element is 1:1, which results from the low amount of the formed MoS_2 in the composite.

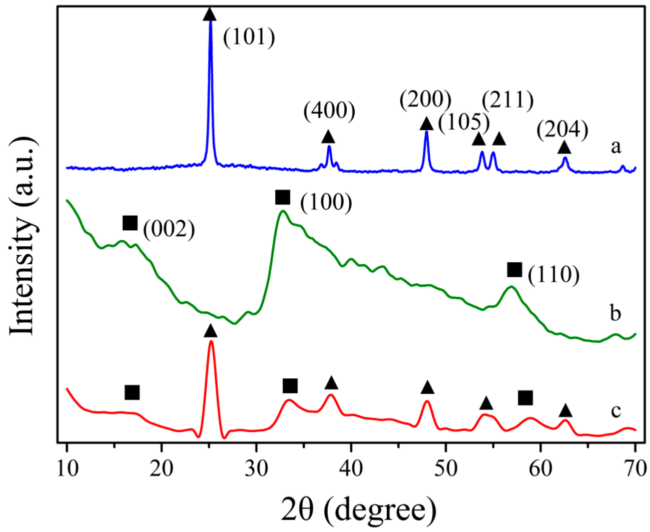

Figure 1. XRD patterns of: TiO_2 nanobelts (NBs) (a); MoS_2 nanotubes (NTs) (b); and MoS_2/TiO_2 heterojunction (c). ▲, denotes the diffraction peak of TiO_2 NBs; ■, the diffraction peak of MoS_2 NTs.

The morphologies of the as-synthesized TiO_2 NBs, MoS_2, and MoS_2/TiO_2 NBs samples are present in Figure 2. It is observed that the formation of $H_2Ti_3O_7$ is uniform nanobelts with smooth surface in Figure 2a, whereas morphology and surface smoothness of the prepared TiO_2 NBs were obviously changed because of dehydration at elevated temperature. Nevertheless, the rough surface of TiO_2 NBs is beneficial for deposition of MoS_2 precursors on the surface of TiO_2 NBs. Meanwhile, in the absence of TiO_2 NBs during the preparation procedure, it was found that uniform MoS_2 nanotubes were formed, which does not agree well with the previous reports on prepared of layered MoS_2 [32–34]. We elucidate that octylamine and ethanol were chosen as combined solvent, which results in curling growth of MoS_2 layers and formation of nanotubes. In the case of MoS_2/TiO_2 NBs composites, the change of TiO_2 NBs morphology is negligible when MoS_2 was formed by hydrothermal process, as displayed in Figure 2d. The MoS_2 anchored on the surface of TiO_2 NBs, which ensures efficient interaction between MoS_2 and TiO_2 NBs. Furthermore, TEM images of these samples were taken to further investigate morphologies and nanostructures, as shown in Figure 3. After annealed at 600 °C for 2 h, the dimension of TiO_2 NBs was reduced by compared with the scale of $H_2Ti_3O_7$ nanobelts owing to releasing of crystal water from the $H_2Ti_3O_7$ lattice, results in shrinking of lattice frame and forming smaller nanobelt pieces with rough surface. In Figure 3c,d, it is observed that the MoS_2 grew on the surface of TiO_2 NBs and formed MoS_2/TiO_2 NBs heterojunction at the interface, which could promote excited charge transportation between MoS_2 and TiO_2 NBs. In addition, we found that when TiO_2 NBs was added as a precursor, the MoS_2 nanotubes were not formed in comparison with the pristine MoS_2 nanotubes in Figure 3b, which indicates that the TiO_2 NBs acts as a solid interface to reduce the curling trend of MoS_2 layers deriving from different polar solvents.

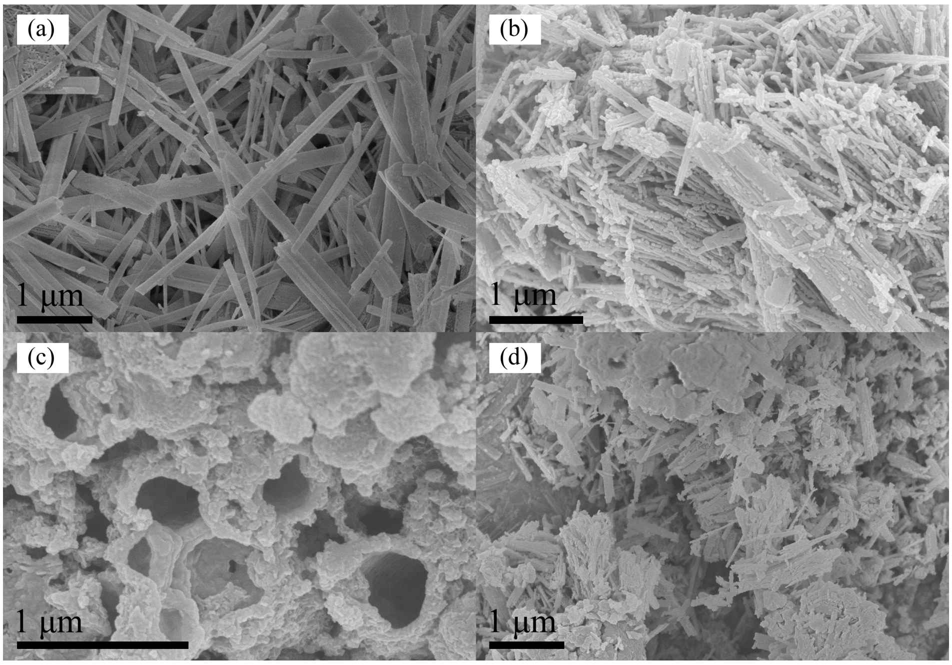

Figure 2. Scanning Electron Microscopy (SEM) images of: $H_2Ti_3O_7$ NBs (**a**); TiO_2 NBs (**b**); MoS_2 nanotubes (**c**); and MoS_2/TiO_2 NBs heterojunctions (**d**).

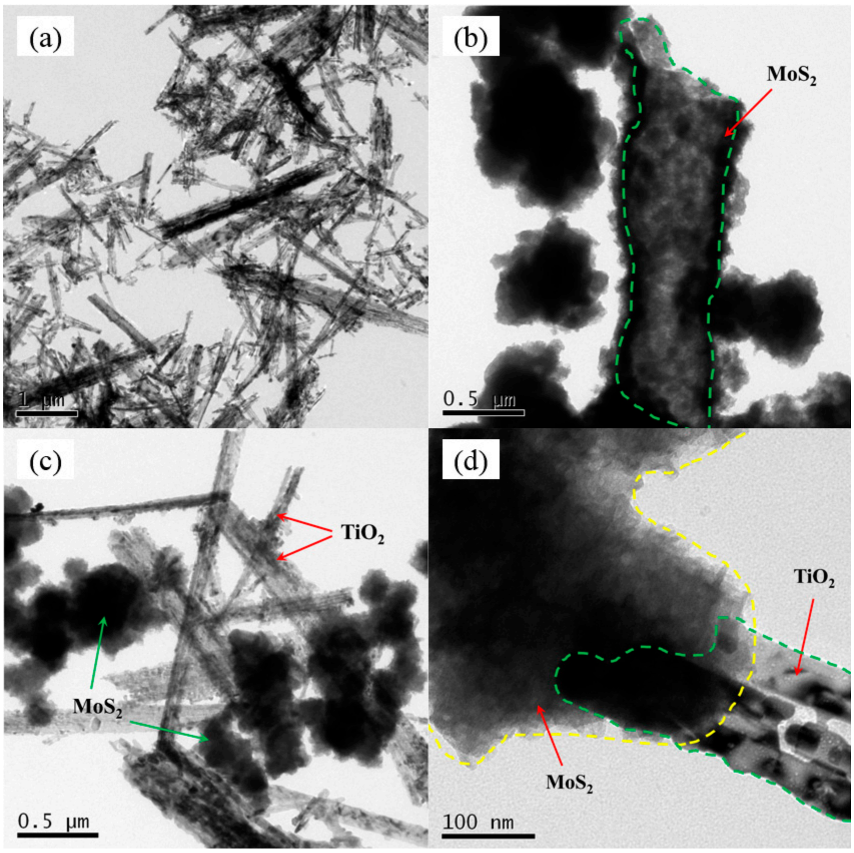

Figure 3. Transmission electron microscopy (TEM) images of: TiO_2 NBs (**a**); MoS_2 (**b**); and MoS_2/TiO_2 NBs (**c**,**d**).

In Figure 4, it is observed that the obvious peaks at 143, 397, and 515 cm^{-1} are attributed to the characteristic $E_{g(1)}$, $B_{1g(1)}$, and A_{1g} + $B_{1g(2)}$ vibration of anatase TiO_2, respectively [26]. In the case of MoS_2, the peaks at 375 and 405 cm^{-1} are ascribed to the typical E^1_{2g} and A_{1g} vibration modes, respectively [31]. It is well-known that the E^1_{2g} vibration mode associates with in-layer displacements of Mo and S atoms while A_{1g} is related to out of layer symmetric displacements of S atoms along *c* axis. The other three obvious peaks at 282, 146, and 336 cm^{-1} originate from E_{1g} and appearance of 1T-MoS_2 phase [35,36]. After epitaxial growth of MoS_2 on the surface of TiO_2 NBs, the corresponding characteristic peaks of TiO_2 and MoS_2 in the composite were detected at 150 and 405 cm^{-1}, respectively, which demonstrates that MoS_2/TiO_2 NBs heterojunction composite was successfully prepared. Furthermore, FTIR spectra of the obtained composite samples are displayed in Figure 5, where the surface organic groups of TiO_2 NBs, MoS_2, and MoS_2/TiO_2 samples have been investigated. The obvious peaks centered at 2920 and 2856 cm^{-1}, and 1502 cm^{-1} are attributed to stretching vibration of C–H and N–H bands from CH_3– and NH_2– because of usage of octylamine as a solvent [37,38]. The characteristic peak at 920 cm^{-1} is assigned to vibration of Mo–S band, which was not found in the pristine TiO_2 NBs sample [39]. In addition, the strong absorbance peak at 472 cm^{-1} was observed, which originates from vibration of Ti–O supported by the previous reports [40]. The above results demonstrate that MoS_2 and TiO_2 phase exist together in the MoS_2/TiO_2 composite.

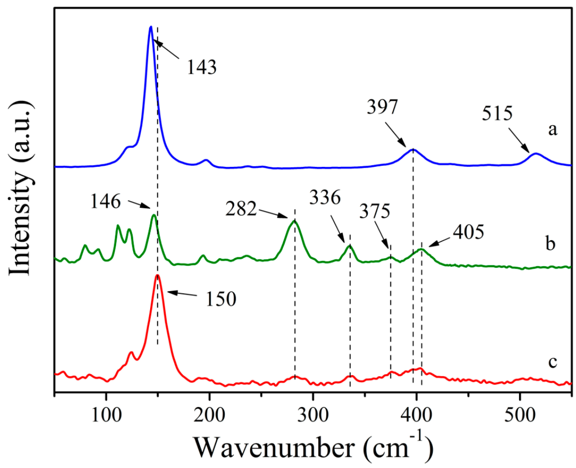

Figure 4. Raman spectra of the: TiO_2 (a); MoS_2 (b); and MoS_2/TiO_2 (c).

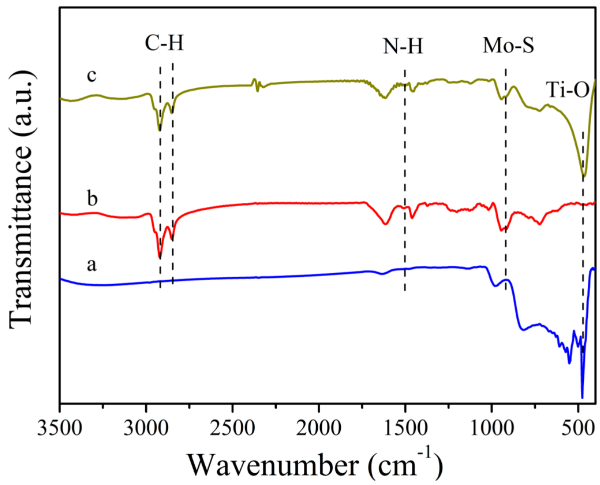

Figure 5. FTIR spectra of the as-prepared TiO_2 NBs (a), MoS_2 (b), and MoS_2/TiO_2 NBs (c) heterojunction.

The X-ray photoelectron spectroscopy (XPS) can probe chemical environment of element in composite, which is useful for investigating composition of MoS_2/TiO_2 heterojunction system. As can be seen in Figure 6a, Mo, Ti, O, and S were obviously observed in survey spectrum of the MoS_2/TiO_2 heterojunction composite, which indicates that the four elements exist in the sample. In the high resolution XPS spectrum of Ti 2p (Figure 6b), two strong peaks, appearing at 459.1 and 464.8 eV, are ascribed to Ti $2p_{3/2}$ and Ti $2p_{1/2}$ of Ti^{4+} in the sample, respectively [41,42]. In Figure 6c, we can observe that the high resolution XPS spectrum of Mo 3d reveals two strong peaks at 228.5 and 231.8 eV, corresponding to Mo $3d_{5/2}$ and Mo $3d_{3/2}$, respectively, which evidently demonstrates the valence state of molybdenum element is +4 in the sample of MoS_2/TiO_2 [31]. Meanwhile, an apparent peak at 225.8 eV is assigned to the binding energy of S 2s, which strongly indicates the existence of MoS_2. In Figure 6d, the peak at 161.4 and 162.5 eV can be assigned to S $2p_{3/2}$ and S $2p_{1/2}$ due to spin orbit separation of S element, which suggests the existence of S^{2-} in the final product [21]. In addition, another peak at 169.2 eV was found, which is due to the residual of $SO_4{}^{2-}$ in the product.

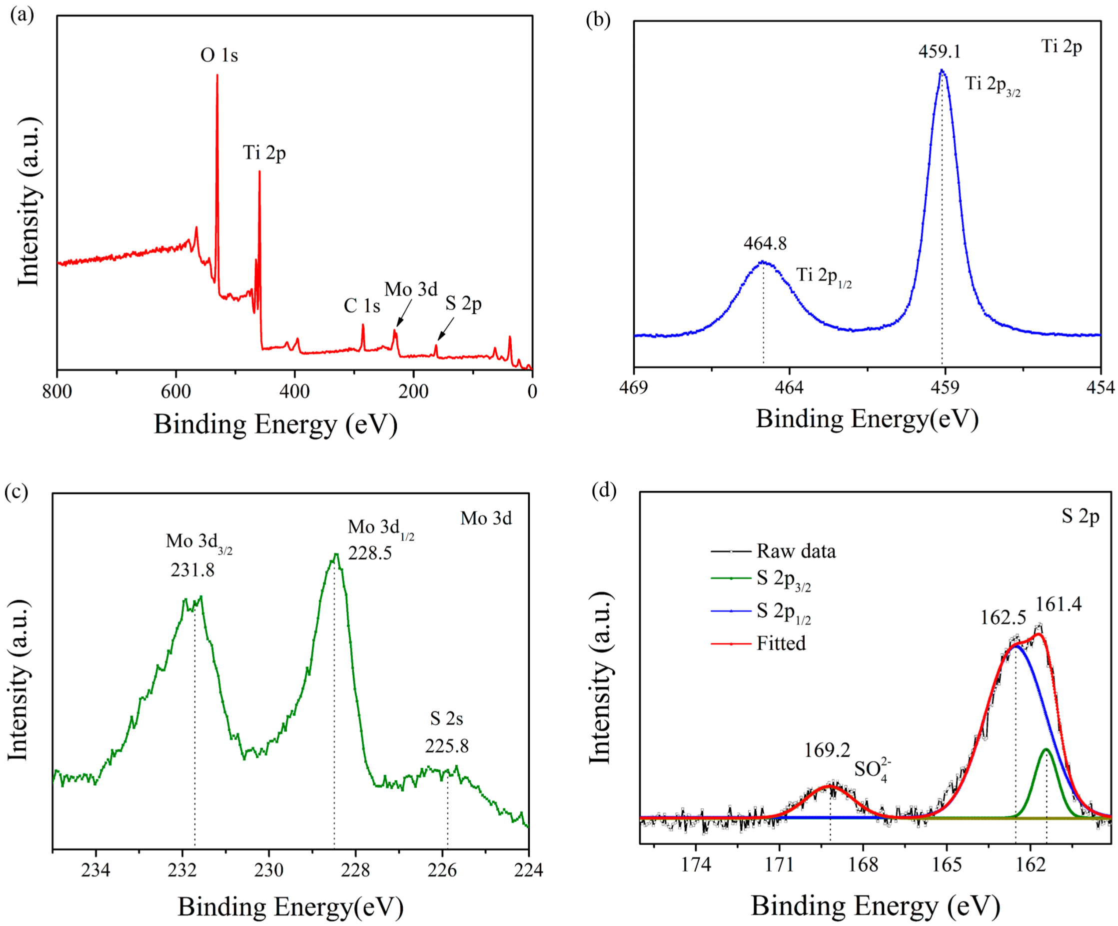

Figure 6. X-ray Photoelectron Spectroscopy (XPS) spectra of: MoS_2/TiO_2, survey (**a**); Ti 2p (**b**); Mo 3d (**c**); and S 2p (**d**).

The UV–vis absorption spectra of the samples are displayed in Figure 7a. The absorption edge of TiO_2 NBs is about 380 nm, which indicates that the pristine TiO_2 NBs only absorbs UV light part of solar light. When coupling with MoS_2, the obtained MoS_2/TiO_2 NBs heterojunction system exhibits strong ability to absorb visible light. Meanwhile, it can be observed that pure MoS_2 possesses excellent photoresponse ability for the entire solar spectrum, which is consistent with the previous report. The optical band gap energy (E_g) of the semiconductors can be calculated from the equation $(\alpha h\nu)^n = A(h\nu - E_g)$ [31], where α, h, ν, E_g, and A are the absorption coefficient, plank constant, light frequency, band gap energy, and a constant, respectively. Among them, n depends on the characteristic of the transition in a semiconductor (n = 2 for direct transition or n = 1/2 for indirect transition). Herein, n is 2 as the material is a direct gap semiconductor. From the plots of $(\alpha h\nu)^2$ vs. $(h\nu)$, the E_g of the TiO_2 NBs, MoS_2, and MoS_2/TiO_2 NBs are about 3.18, 1.30, and 3.07 eV, respectively, as shown in Figure 7b. The result reveals that the light harvesting range of the heterojunction sample is enlarged after coupling TiO_2 NBs with MoS_2.

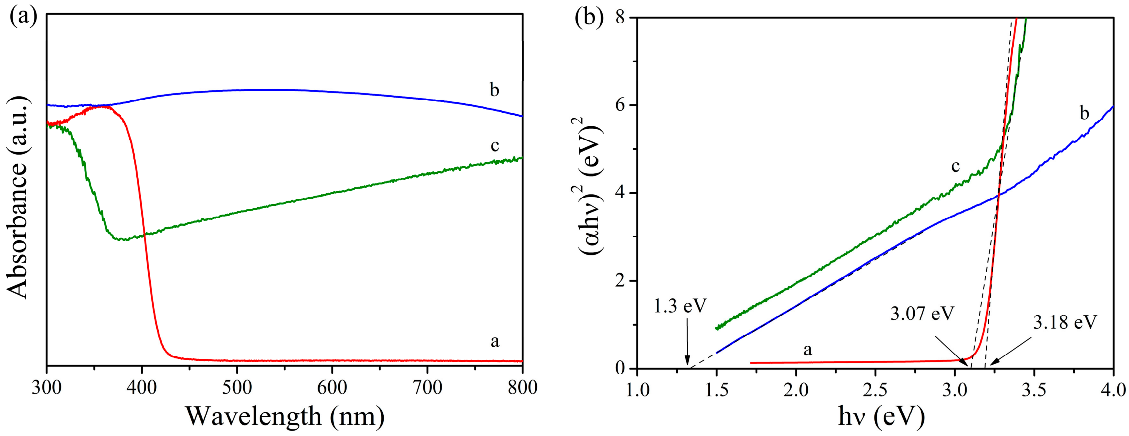

Figure 7. (**a**) UV–visible absorption spectra; and (**b**) Tauc's plots of the as-prepared TiO_2 NBs, MoS_2, and MoS_2/TiO_2 NBs heterojunction.

To evaluate effects of the morphologies of the as-obtained samples on adsorptive performance, N_2 adsorption–desorption isotherm analysis was used to gain the surface area ratio and distribution of pore size. The BET specific surface areas of TiO_2 NBs, MoS_2 and MoS_2/TiO_2 heterojunction were calculated and equal to 46.8, 255.3 and 62.9 m^2/g, respectively. The larger surface area of the pristine MoS_2 sample is due to the unique nanotube structure, which could increase the surface area of TiO_2 NBs after coupling MoS_2 and TiO_2. The corresponding pore size distribution are 2.2, 2.1, and 1.9 nm for the pristine TiO_2 NBs, MoS_2, and MoS_2/TiO_2 heterojunction system, respectively, which shows a similar pore distribution, resulting from the interstitial spaces between nanobelts. The results indicate that the coupling could enlarge the surface area and slightly change the pore size.

2.2. Photocatalytic Activity of MoS_2/TiO_2 NBs Heterojunctions

Owing to different redox potentials of $Cr_2O_7^{2-}$ under different pH conditions [43], effects of pH values on photoactivity of MoS_2/TiO_2 heterojunction system for reducing of Cr(VI) were investigated (Figure 8). It was observed that the adsorption ability of MoS_2/TiO_2 composite for Cr(VI) under acid condition is the similar as under neutral and base condition during dark equilibrium process. However, when the solution was irradiated by visible light, the degradation efficiency of Cr(VI) under acidic condition is much higher than under neutral and alkaline condition, which indicates that acidic condition is beneficial for photoreduction of Cr(VI) over MoS_2/TiO_2 composite. It was found that 100% of Cr(VI) was reduced under acidic condition under irradiation for 1 h. We elucidate that the $Cr_2O_7^{2-}$ ion under acidic condition possesses lower redox potential than under alkaline condition, which ensures photoreduction reaction of Cr(VI) carried out over the MoS_2/TiO_2 composites.

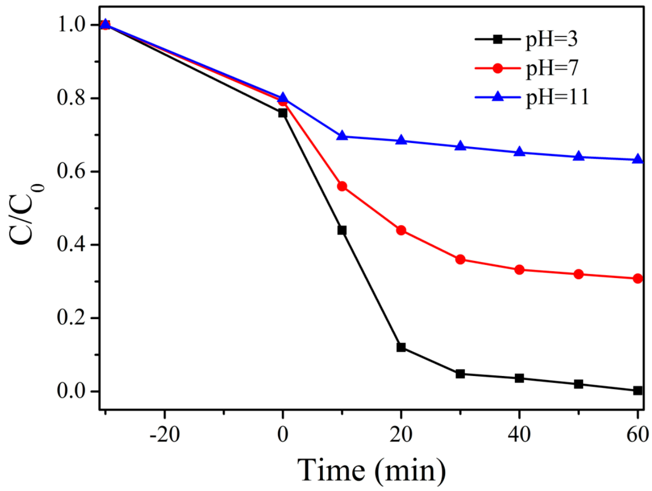

Figure 8. Degradation curves of Cr(VI) over MoS_2/TiO_2 composite under different pH conditions.

Meanwhile, we compared photoreduction efficiency of Cr(VI) over the MoS_2/TiO_2 NBs composite with the pure TiO_2 NBs, pristine MoS_2, and mechanically mixed TiO_2 + MoS_2 samples, as shown in Figure 9. The degradation efficiency of Cr(VI) reached to nearly 100% for the MoS_2/TiO_2 NBs composite, whereas other samples exhibited lower photocatalytic activities during the visible light illumination process. In the case of blank test, the concentration of Cr(VI) has almost no variation under visible light illumination for 1 h, which rules out the photolysis effect on the absorption peak of Cr(VI). Meanwhile, it was found that the mechanically mixed sample MoS_2 + TiO_2 displayed low photoreduction activity even though MoS_2 was added, which demonstrates that the efficient heterojunction has not been formed at the interface between MoS_2 and TiO_2 NBs by mechanical mixing. In addition, the MoS_2 nanotubes present less adsorptive ability of Cr(VI) under adsorption–desorption equilibrium process, which does not agree well with the result of BET specific surface area. We elucidate that although the prepared MoS_2 possesses huge surface area, it cannot chelate with negative $Cr_2O_7^{2-}$ ions, resulting in low adsorbing amount under dark.

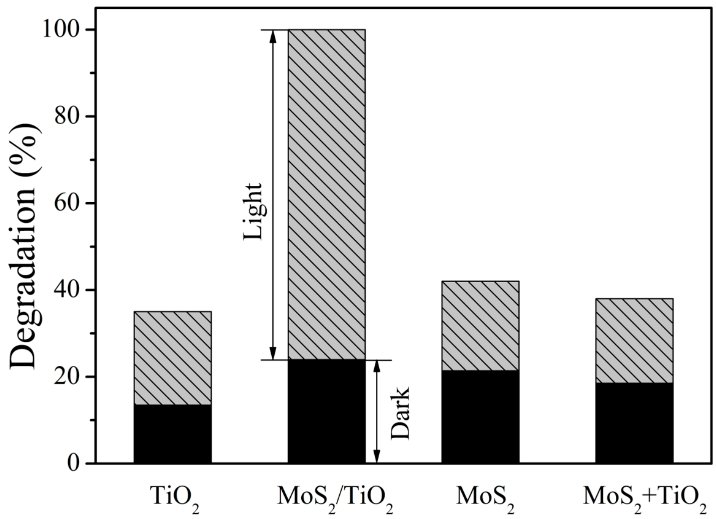

Figure 9. Degradation efficiency of Cr(VI) over the different samples under visible light irradiation.

2.3. Photocatalytic Reduction Mechanism of MoS_2/TiO_2 NBs p-n Heterojunction

Figure 10 exhibits a schematic diagram of the band structure of the pristine *n*-type TiO_2 NBs and *p*-type MoS_2. Commonly, for *n*-type TiO_2, the Fermi level is close to the conduction band, whereas for *p*-type MoS_2, the Fermi level approaches to the valence band. When the TiO_2 NBs was coupled with the MoS_2, the heterojunctions among these semiconductors were formed, resulting in the realignment of their valence and conduction bands due to the thermal equilibrium of different Fermi levels and the formation of built-in electric field [44,45]. This allows the energy bands of TiO_2 and MoS_2 shift downward and upward, respectively, along the Fermi level, as shown in Figure 10. When the MoS_2/TiO_2 heterojunction system was irradiated by visible light, the MoS_2 are excited to produce electrons and holes. The photoinduced electrons on the conduction band of the MoS_2 transfer to that of TiO_2 NBs, whereas the holes remain in the valence band of the MoS_2, which could react with S^{2-} in the sample and to some degree undermine the photocatalytic performance of the sample, as shown in Figure S1. As discussed above, owing to the formation of the heterojunction at the interface between MoS_2 and TiO_2 NBs, the suppression of the recombination of photoinduced electron–hole pairs is realized, which allows more photogenerated electrons to participate in the reduction reactions and strongly enhances photocatalytic activity under visible light irradiation.

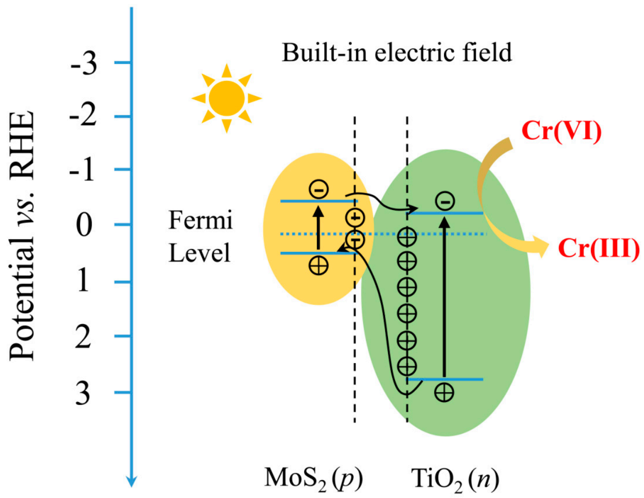

Figure 10. Schematic diagram for energy band of MoS_2/TiO_2 NBs *p-n* heterojunction and photocatalytic reduction mechanism of Cr(VI).

3. Experimental Section

3.1. Synthesis of TiO_2 Nanobelts

First, 0.4 g of P25 powder was added into 80 mL of NaOH solution (10 M), and stirred vigorously for 30 min to obtain mean suspension. The mixture was transferred to 100 mL Teflon autoclave, which was heated to 180 °C and maintained for 48 h. After that, a white product, $Na_2Ti_3O_7$, was collected and washed by deionized water. Then the white product was added into HCl solution (0.1 M) and stirred for 24 h to gain $H_2Ti_3O_7$. The product was dispersed into 80 mL of 0.02 M H_2SO_4 and then transferred into Teflon autoclave, kept at 100 °C for 24 h. The white product was centrifuged, washed by purified water, and dried at 70 °C for overnight. Finally, the TiO_2 nanobelt was produced after calcination at 600 °C for 2 h.

3.2. Synthesis of MoS_2/TiO_2 NBs Heterojunction

In typical procedure, 0.042 g of roughly TiO_2 NBs, 0.265 g of ammonium molybdate tetrahydrate, and 0.11 g of sulfur powder were dispersed into 38 mL of absolute ethanol and 40 mL of octylamine, stirred vigorously for 30 min. Then the mixture was transferred into 100 mL Teflon autoclave, and kept at 180 °C for 24 h. After cooled to room temperature, the sample was obtained by centrifuging and washed by deionized water. The sample was dried at 70 °C for 24 h, denoted as MoS_2/TiO_2 heterojunction.

3.3. Characterizations

X-ray powder diffraction (XRD) was carried out on Shimadzu LabX-6000 (Cu Kα = 1.5406 Å) (Shimadzu, Kyoto, Japan). Scanning electron microscopy (SEM) images were taken on a JSM-6700LV operated at 5.0 kV (JEOL Ltd., Tokyo, Japan). Transmission electron microscopy (TEM) images were recorded on a Philips Tecnai 20 electron microscope (FEI, Hillsboro, OR, USA). UV–vis diffuse reflectance spectra (DRS) were recorded on a UV–vis spectrophotometer (UV1100, Tianmei, Shanghai, China). Raman and FTIR spectra were carried out in Laser Confocal Microscopy Raman Spectrometer (Thermo Fisher Scientific DXR, Waltham, MA, USA) and Bruker V70 (Bruker, Ettlingen, Germany), respectively. X ray photoelectron spectroscopy (XPS) data that determined the chemical composition of MoS_2/TiO_2 NBs powder were recorded with a PerkinElmer PHI 5600 electron spectrometer (PerkinElmer, Waltham, MA, USA).

3.4. Photocatalytic Activity Measurement

The photocatalytic activities of the samples were tested by the photocatalytic reduction of Cr(VI), and a 300 W Xe lamp with a 400 nm cut-off filter was used as the light resource. In a typical photocatalytic procedure, 0.05 g of the as-obtained sample was added into 100 mL of Cr(VI) solution (25 $mg \cdot L^{-1}$). The suspensions were stirred in the dark for 0.5 h to reach an adsorption–desorption equilibrium before exposed to irradiation. Then, the solution was exposed to light irradiation under magnetic stirring. At each given time interval, 3 mL suspension was sampled and centrifuged to remove the solid. The concentration of Cr(VI) during the degradation was monitored by colorimetry using a UV1100 spectrophotometer. All of the measurements were carried out at room temperature.

4. Conclusions

In this work, we successfully synthesized MoS_2/TiO_2 nanobelt heterojunction by in situ growth of MoS_2 on the surface of TiO_2 NBs. The photocatalytic reduction of Cr(VI) reveals that the synthesized MoS_2/TiO_2 NBs composite have superior photocatalytic ability than other samples. As a result of special energy level offset and nanostructure, MoS_2/TiO_2 NBs composite were endowed with higher light-harvesting capacity and charge transportation efficiency, which are indispensible merits for excellent photocatalytic activity. Meanwhile, a photoreduction mechanism is proposed based on the systematic investigation, where the photogenerated electrons are demonstrated as the dominant reductive species to reduce Cr(VI) to Cr(III).

Supplementary Materials: The following are available online at www.mdpi.com/2073-4344/7/1/30/s1, Figure S1: The recycling runs for photoreduction of Cr(VI) in the presence of the MoS_2/TiO_2 nanotubes (NTs) sample.

Acknowledgments: This work was supported financially by the National Natural Science Foundation of China (21507029, 21501138, and 51379077), the Natural Science Foundation of Hubei Province (2015CFB177), China Ministry of Education and the Fundamental Research Funds for the Central Universities (2016MS109), Nature Science Foundation of Hebei Province (B2016502063), Open Foundation of Key Laboratory of Industrial Ecology and Environmental Engineering (KLIEEE-15-02), and China Ministry of Education and the Fundamental Research Funds for the Central Universities (2016MS109).

Author Contributions: Jie Liu and Jun Ke conceived and designed experiments; Jie Liu and Ying Li performed the experiment and analyzed the data; Zhong Wang contributed to some part of characterizations; Jie Liu and Jun Ke wrote the manuscript; Huining Xiao and Jun Ke contributed to revise the manuscript.

Conflicts of Interest: The authors declare no conflict of interest.

References

1. Zhang, R.N.; Pan, X.H.; Li, F.; Zhang, L.; Zhai, S.M.; Mu, Q.X.; Liu, J.F.; Qu, G.B.; Jiang, G.B.; Yan, B. Cell rescue by nanosequestration: Reduced cytotoxicity of an environmental remediation residue, $Mg(OH)_2$ nanoflake/Cr(VI) adduct. *Environ. Sci. Technol.* **2014**, *48*, 1984–1992. [CrossRef] [PubMed]
2. Bokare, A.D.; Choi, W. Advanced oxidation process based on the Cr(III)/Cr(VI) redox cycle. *Environ. Sci. Technol.* **2011**, *45*, 9332–9338. [CrossRef] [PubMed]
3. Hsu, L.C.; Wang, S.L.; Lin, Y.C.; Wang, M.K.; Chiang, P.N.; Liu, J.C.; Kuan, W.H.; Chen, C.C.; Tzou, Y.M. Cr(VI) removal on fungal biomass of *Neurospora crassa*: The importance of dissolved organic carbons derived from the biomass to Cr(VI) reduction. *Environ. Sci. Technol.* **2010**, *44*, 6202–6208. [CrossRef] [PubMed]
4. Wang, L.; Li, X.Y.; Teng, W.; Zhao, Q.D.; Shi, Y.; Yue, R.L.; Chen, Y.F. Efficient photocatalytic reduction of aqueous Cr(VI) over flower-like $SnIn_4S_8$ microspheres under visible light illumination. *J. Hazard. Mater.* **2013**, *244*, 681–688. [CrossRef] [PubMed]
5. Chu, H.P.; Lei, W.Y.; Liu, X.J.; Li, J.L.; Zheng, W.; Zhu, G.; Li, C.; Pan, L.K.; Sun, C.Q. Synergetic effect of TiO_2 as co-catalyst for enhanced visible light photocatalytic reduction of Cr(VI) on $MoSe_2$. *Appl. Catal. A* **2016**, *521*, 19–25. [CrossRef]
6. Wang, H.G.; Wen, F.F.; Li, X.Y.; Gan, X.R.; Yang, Y.N.; Chen, P.; Zhang, Y. Cerium-doped MoS_2 nanostructures: Efficient visible photocatalysis for Cr(VI) removal. *Sep. Purif. Technol.* **2016**, *170*, 190–198. [CrossRef]
7. Yang, D.; Sun, Y.Y.; Tong, Z.W.; Nan, Y.H.; Jiang, Z.Y. Fabrication of bimodal-pore $SrTiO_3$ microspheres with excellent photocatalytic performance for Cr(VI) reduction under simulated sunlight. *J. Hazard. Mater.* **2016**, *312*, 45–54. [CrossRef] [PubMed]
8. Baudys, M.; Krysa, J.; Zlamal, M.; Mills, A. Weathering tests of photocatalytic facade paints containing ZnO and TiO_2. *Chem. Eng. J.* **2015**, *261*, 83–87. [CrossRef]
9. Chen, H.H.; Nanayakkara, C.E.; Grassian, V.H. Titanium dioxide photocatalysis in atmospheric chemistry. *Chem. Rev.* **2012**, *112*, 5919–5948. [CrossRef] [PubMed]
10. Hong, J.Y.; Bae, S.E.; Won, Y.S.; Huh, S. Simple preparation of lotus-root shaped meso-/macroporous TiO_2 and their DSSC performances. *J. Colloid Interface Sci.* **2015**, *448*, 467–472. [CrossRef] [PubMed]
11. Chen, J.; Zhao, D.W.; Li, C.; Xu, F.; Lei, W.; Sun, L.T.; Nathan, A.; Sun, X.W. All solution-processed stable white quantum dot light emitting diodes with hybrid ZnO@TiO_2 as blue emitters. *Sci. Rep.* **2014**, *4*, 4085. [CrossRef] [PubMed]
12. Guo, B.J.; Yu, K.; Fu, H.; Hua, Q.Q.; Qi, R.J.; Li, H.L.; Song, H.L.; Guo, S.; Zhu, Z.Q. Firework-shaped TiO_2 microspheres embedded with few-layer MoS_2 as an anode material for excellent performance lithium-ion batteries. *J. Mater. Chem. A* **2015**, *3*, 6392–6401. [CrossRef]
13. Tosoni, S.; Hevia, D.F.; Diaz, O.G.; Illas, F. Origin of optical excitations in fluorine-doped titania from response function theory: Relevance to photocatalysis. *J. Phys. Chem. Lett.* **2012**, *3*, 2269–2274. [CrossRef] [PubMed]
14. Xu, L.M.; Ming, L.F.; Chen, F. TiO_2 with "fluorine-occupied" surface oxygen vacancies and its stably enhanced photocatalytic performance. *ChemCatChem* **2015**, *7*, 1797–1800. [CrossRef]
15. Chen, Q.F.; Ma, W.H.; Chen, C.C.; Ji, H.W.; Zhao, J.C. Anatase TiO_2 mesocrystals enclosed by (001) and (101) facets: Synergistic effects between Ti^{3+} and facets for their photocatalytic performance. *Chem. Eur. J.* **2012**, *18*, 12584–12589. [CrossRef] [PubMed]
16. Ruoko, T.; Kaunisto, K.; Bartsch, M.; Pohjola, J.; Hiltunen, A.; Niederberger, M.; Tkachenko, N.V.; Lemmetyinen, H. Subpicosecond to second time-scale charge carrier kinetics in hematite-titania nanocomposite photoanodes. *J. Phys. Chem. Lett.* **2015**, *6*, 2859–2864. [CrossRef] [PubMed]
17. Skorb, K.V.; Antonouskaya, L.I.; Belyasova, N.A.; Shchukin, D.G.; Mohwald, H.; Sviridov, D.V. Antibacterial activity of thin film photocatalysts based on metal modified TiO_2 and TiO_2: In_2O_3 nanocomposite. *Appl. Catal. B* **2008**, *84*, 94–99. [CrossRef]
18. Ahmad, W.; Noor, T.; Zeeshan, M. Effect of synthesis route on catalytic properties and performance of Co_3O_4/TiO_2 for carbon monoxide and hydrocarbon oxidation under real engine operating conditions. *Catal. Commun.* **2017**, *89*, 19–24. [CrossRef]
19. Yu, X.; Zhang, J.; Zhao, Z.H.; Guo, W.B.; Qiu, J.C.; Mou, X.N.; Li, A.X.; Claverie, J.P.; Liu, H. NiO–TiO_2 *p-n* heterostructured nanocables bridged by zero-bandgap rGO for highly efficient photocatalytic water splitting. *Nano Energy* **2015**, *16*, 207–217. [CrossRef]

20. Zhou, W.J.; Yin, Z.Y.; Du, Y.P.; Huang, X.; Zeng, Z.Y.; Fan, Z.X.; Liu, H.; Wang, J.Y.; Zhang, H. Synthesis of few layer MoS_2 nanosheet coated TiO_2 nanobelt heterostructures for enhanced photocatalytic activities. *Small* **2013**, *9*, 140–147. [CrossRef] [PubMed]
21. Weng, B.; Zhang, X.; Zhang, N.; Tang, Z.R.; Xu, Y.J. Two-dimensional MoS_2 nanosheet-coated Bi_2S_3 discoids: Synthesis, formation mechanism, and photocatalytic application. *Langmuir* **2015**, *31*, 4314–4322. [CrossRef] [PubMed]
22. Li, H.L.; Yu, K.; Lei, X.; Guo, B.J.; Li, C.; Fu, H.; Zhu, Z.Q. Synthesis of the MoS_2@CuO heterogeneous structure with improved photocatalysis performance and H_2O adsorption analysis. *Dalton Trans.* **2015**, *44*, 10438–10447. [CrossRef] [PubMed]
23. Duan, K.Y.; Du, Y.L.; Feng, Q.L.; Ye, X.L.; Xie, H.; Xue, M.Y.; Wang, C.M. Synthesis of platinum nanoparticles by using molybdenum disulfide as a template and its application to enzyme-like catalysis. *ChemCatChem* **2014**, *6*, 1873–1876. [CrossRef]
24. Zong, X.; Yan, H.J.; Wu, G.P.; Ma, G.J.; Wen, F.Y.; Wang, L.; Li, C. Enhancement of photocatalytic H_2 evolution on CdS by loading MoS_2 as cocatalyst under visible light irradiation. *J. Am. Chem. Soc.* **2008**, *130*, 7176–7177. [CrossRef] [PubMed]
25. Zhu, B.L.; Lin, B.Z.; Zhou, Y.; Sun, P.; Yao, Q.R.; Chen, Y.L.; Gao, B.F. Enhanced photocatalytic H_2 evolution on ZnS loaded with graphene and MoS_2 nanosheets as cocatalysts. *J. Mater. Chem. A* **2014**, *2*, 3819–3827. [CrossRef]
26. Shen, M.; Yan, Z.P.; Yang, L.; Du, P.W.; Zhang, J.Y.; Xiang, B. MoS_2 nanosheet/TiO_2 nanowire hybrid nanostructures for enhanced visible-light photocatalytic activities. *Chem. Commun.* **2014**, *50*, 15447–15449. [CrossRef] [PubMed]
27. Lu, Z.Y.; Zhang, H.C.; Zhu, W.; Yu, X.Y.; Kuang, Y.; Chang, Z.; Lei, X.D.; Sun, X.M. In situ fabrication of porous MoS_2 thin films as high performance catalysts for electrochemical hydrogen evolution. *Chem. Commun.* **2013**, *49*, 7516–7518. [CrossRef] [PubMed]
28. Sun, S.C.; Gao, P.; Yang, Y.R.; Yang, P.P.; Chen, Y.J.; Wang, Y.B. N-doped TiO_2 nanobelts with coexposed (001) and (101) facets and their highly efficient visible-light-driven photocatalytic hydrogen production. *ACS Appl. Mater. Interfaces* **2016**, *8*, 18126–18131. [CrossRef] [PubMed]
29. Wu, N.Q.; Wang, J.; Tafen, D.N.; Wang, H.; Zheng, J.G.; Lewis, J.P.; Liu, X.G.; Leonard, S.S.; Manivannan, A. Shape enhanced photocatalytic activity of single-crystalline anatase TiO_2 (101) nanobelts. *J. Am. Chem. Soc.* **2010**, *132*, 6679–6685. [CrossRef] [PubMed]
30. Li, X.D.; Li, W.; Li, M.C.; Cui, P.; Chen, D.H.; Genenbach, T.; Chu, L.H.; Liu, H.Y.; Song, G.S. Glucose-assisted synthesis of the hierarchical TiO_2 nanowire@MoS_2 nanosheet nanocomposite and its synergistic lithium storage performance. *J. Mater. Chem. A* **2015**, *3*, 2762–2769. [CrossRef]
31. Ke, J.; Liu, J.; Sun, H.Q.; Zhang, H.Y.; Duan, X.G.; Liang, P.; Li, X.Y.; Tade, M.; Liu, S.M.; Wang, S.B. Facile assembly of Bi_2O_3/Bi_2S_3/MoS_2 *n-p* heterojunction with layered *n*-Bi_2O_3 and *p*-MoS_2 for enhanced photocatalytic water oxidation and pollutant degradation. *Appl. Catal. B* **2017**, *200*, 47–55. [CrossRef]
32. Hou, Y.; Zhang, B.; Wen, Z.H.; Cui, S.M.; Guo, X.R.; He, Z.; Chen, J.H. A 3D hybrid of layered MoS_2/nitrogen-doped graphene nanosheet aerogels: An effective catalyst for hydrogen evolution in microbial electrolysis cells. *J. Mater. Chem. A* **2014**, *2*, 13795–13800. [CrossRef]
33. Zhao, X.; Zhu, H.; Yang, X.R. Amorphous carbon supported MoS_2 nanosheets as effective catalysts for electrocatalytic hydrogen evolution. *Nanoscale* **2014**, *6*, 10680–10685. [CrossRef] [PubMed]
34. Al-Mamun, M.; Zhang, H.M.; Liu, P.R.; Wang, Y.; Cao, J.; Zhao, H.J. Directly hydrothermal growth of ultrathin MoS_2 nanostructured films as high performance counter electrodes for dye-sensitised solar cells. *RSC Adv.* **2014**, *4*, 21277–21283. [CrossRef]
35. Lukowski, M.A.; Daniel, A.S.; Meng, F.; Forticaux, A.; Li, L.S.; Jin, S. Enhanced hydrogen evolution catalysis from chemically exfoliated metallic MoS_2 nanosheets. *J. Am. Chem. Soc.* **2013**, *135*, 10274–10277. [CrossRef] [PubMed]
36. Cai, L.; He, J.F.; Liu, Q.H.; Yao, T.; Chen, L.; Yan, W.S.; Hu, F.C.; Jiang, Y.; Zhao, Y.D.; Hu, T.D.; et al. Vacancy-induced ferromagnetism of MoS_2 nanosheets. *J. Am. Chem. Soc.* **2015**, *137*, 2622–2627. [CrossRef] [PubMed]
37. Ndokoye, P.; Ke, J.; Liu, J.; Zhao, Q.D.; Li, X.Y. L-Cysteine-modified gold nanostars for SERS-based copper ions detection in aqueous media. *Langmuir* **2014**, *30*, 13491–13497. [CrossRef] [PubMed]

38. Ke, J.; Li, X.Y.; Zhao, Q.D.; Hou, Y.; Chen, J.H. Ultrasensitive quantum dot fluorescence quenching assay for selective detection of mercury ions in drinking water. *Sci. Rep.* **2014**, *4*, 5624. [CrossRef] [PubMed]
39. Wang, X.H.; Ding, J.J.; Yao, S.W.; Wu, X.X.; Feng, Q.Q.; Wang, Z.H.; Geng, B.Y. High supercapacitor and adsorption behaviors of flower-like MoS_2 nanostructures. *J. Mater. Chem. A* **2014**, *2*, 15958–15963. [CrossRef]
40. Jiang, Z.Y.; Liu, Y.Y.; Jiang, T.; Huang, B.B.; Wang, Y.Y.; Zhang, X.Y.; Qin, X.Y.; Dai, Y. Enhancing visible light photocatalytic activity of TiO_2 using a colorless molecule (2-methoxyethanol) due to hydrogen bond effect. *Appl. Catal. B* **2017**, *200*, 230–236. [CrossRef]
41. Liu, J.M.; Han, L.; An, N.; Xing, L.; Cheng, L.; Yang, J.C.; Zhang, Q.C. Enhanced visible light photocatalytic activity of carbonate doped anatase TiO_2 based on the electron withdrawing bidentate carboxylate linkage. *Appl. Catal. B* **2017**, *202*, 642–652. [CrossRef]
42. Wei, N.; Cui, H.Z.; Song, Q.; Zhang, L.Q.; Song, X.J.; Wang, K.; Zhang, Y.F.; Li, J.; Wen, J.; Tian, J. Ag_2O nanoparticle/TiO_2 nanobelt heterostructures with remarkable photo-response and photocatalytic properties under UV, visible and near-infrared irradiation. *Appl. Catal. B* **2016**, *198*, 83–90. [CrossRef]
43. Wang, C.C.; Du, X.D.; Guo, X.X.; Wang, P.; Zhang, J. Photocatalytic Cr(VI) reduction in metal-organic frameworks: A mini-review. *Appl. Catal. B* **2016**, *193*, 198–216. [CrossRef]
44. Sun, J.J.; Li, X.Y.; Zhao, Q.D.; Ke, J.; Zhang, D.K. Novel $V_2O_5/BiVO_4/TiO_2$ nanocomposites with high visible light induced photocatalytic activity for the degradation of toluene. *J. Phys. Chem. C* **2014**, *118*, 10113–10121. [CrossRef]
45. Peng, Y.; Yan, M.; Chen, Q.G.; Fan, C.M.; Zhou, H.Y.; Xu, A.W. Novel one dimensional Bi_2O_3-Bi_2WO_6 *p-n* hierarchical heterojunction with enhanced photocatalytic activity. *J. Mater. Chem. A* **2014**, *2*, 8517–8524. [CrossRef]